Mechanical Systems and Signal Processing 158 (2021) 107749

Contents lists available at ScienceDirect

Mechanical Systems and Signal Processing

journal homepage: www.elsevier.com/locate/ymssp

Assessment and prediction of high speed railway bridge long-term deformation based on track geometry inspection big data

Yuan Wang [a], Ping Wang [b], Huiyue Tang [c,d], Xiang Liu [e], Jinhui Xu [f], Jieling Xiao [b,*], Jingshen Wu [a]

[a] School of System Design and Intelligent Manufacturing, Southern University of Science and Technology, Shenzhen, PR China
[b] Key Laboratory of High-speed Railway Engineering, Ministry of Education, Chengdu, PR China
[c] Institute of Robotics and Intelligent Manufacturing, The Chinese University of Hong Kong, Shenzhen, PR China
[d] Shenzhen Institute of Artificial Intelligence and Robotics for Society, Shenzhen, PR China
[e] Department of Civil and Environmental Engineering, Rutgers, The State University of New Jersey, NJ, USA
[f] Department of Civil and Architecture Engineering, East China Jiaotong University, Nanchang, PR China

ARTICLE INFO

Article history:
Received 5 June 2018
Received in revised form 29 May 2020
Accepted 10 February 2021

Keywords:
High speed railway
Track geometry inspection
Bridge deformation assessment
Prediction
Signal processing

ABSTRACT

This paper proposes a low-cost, data-driven approach to assess and predict bridge deformation using track inspection big data, which is primarily used for assessing track conditions. Firstly, a Bridge Deformation Assessment model with a sophisticated signal processing process is introduced to manipulate track geometry inspection data for extracting bridge-related components. Secondly, a Bridge Dynamical Deformation index (BDD index) is defined to quantify bridge deformation based on track geometry inspection data. Thirdly, the Temperature-Time-Deformation model (TTD model) is established to describe bridge deformation with respect to ambient temperature and length of service time of the bridge. Three types of TTD equations are proposed, including exponential-, hyperbolic- and linear-TTD equations. Fourthly, a track geometry inspection dataset over 2.6 years involving 563 bridge spans is applied as a case study. It is found that the BDD index changes with ambient temperature by 0.02 mm/°C on average, and increases with time by 0.2 mm/year during the 2.6-year period. Furthermore, a prediction on the amount of increase of the BDD index over the following 3 years is given with a 95% confidence level. It is expected that BDD index will increase by 0.5 mm in 2 years and 0.7 mm in 3 years according to the TTD model. Finally, the model uncertainty is discussed from data aspect and model aspect. The methods in this paper are of reference value for research topics on bridge condition evolution, rail geometry degradation and prediction-based infrastructure maintenance.

1. Introduction

1.1. Background

Bridge-based sections account for a large proportion of China's High-Speed Railways (HSR) due to their advantages of avoiding the interruption of existing lines and the occupation of land [1–3]. As a result, the demand for assessment of the condition of such a large amount of bridges over the long term is steadily increasing. Among different bridge types, the sim-

* Corresponding author.
E-mail address: xjling@swjtu.edu.cn (J. Xiao).

https://doi.org/10.1016/j.ymssp.2021.107749
0888-3270/

ply supported beam accounts for the largest proportion [3]. This paper focuses on the condition of simply supported beams; the bridge and track layout information are given in Section 1.2.

Bridge condition simulation, evaluation, prediction, and condition monitoring [4–7,71,72] has long been a hot topic, especially for high-speed railway lines [8–43]. One universal and widespread concern is bridge deformation [25–43], including deflection (downward bend) and camber (upward bend). Large bridge deformation will cause a larger rotation angle between any two adjacent bridges spans, leading to defects in the longitudinal profile of the track and reducing the running stability, comfort and safety of the trains [21–22,43].

Bridge deformation can be divided into three categories: (1) temporary deformation (TD), (2) periodical deformation (PD) and (3) time-developing deformation (TDD). TD is the recoverable deflection caused by trainloads, and it will restore when the train load is no longer present. PD refers to deformation which changes periodically due to ambient climatic conditions, such as the thermal gradients of bridge cross sections [47–57]. In the time scale of one year, PD shows seasonal fluctuation characteristics. TDD is the unrecoverable deformation which evolves gradually over a long time. The most important factors causing TDD are the loss of reinforcement prestress [26,29,30,44–46] and the creep and shrinkage of concrete [23,31–37,46]. Fig. 1 presents illustration of TD, PD and TDD. A brief literature review about TD, PD and TRD is given in Section 2.

This paper does not aim to study the mechanism of TD, PD and TDD. Instead, the objective of this paper is to introduce a novel data analysis approach for assessment and prediction of railway bridge deformation over the long term using big data from track inspection. The measured data and the measurement principle of track inspection cars are introduced in Section 1.3.

1.2. Bridge-based track layout

In this paper, our special interest is on bridge deformation. The China High-Speed Railway track geometry inspection dataset from Jan. 2015 to Aug. 2017 is used as a case study in this paper. The construction of the railway line began on Dec. 30, 2008. The design speed is 250 km/h. The line began operation on Jan. 1, 2015. It is reported that the bridge girders were placed on the piers around June 2010. The track is a CRTS I slab track. As illustrated in Fig. 2, the bridge type is reinforced concrete pre-stressed box girder with length of 32 m. There are two lengths of slabs, one is 5 m (Slab 2 in Fig. 2) and the other is 3.8 m (Slab 1 in Fig. 2), with the order of 3.8 + 5 + 5 + 5 + 5 + 5 + 3.8 = 32.6 m. The slabs don't lie across two girders. Note that the actual spatial period of one single simple supported bridge is 32 m + 0.3 m + 0.3 m + 0.1 m = 32.7 m. For the bridge girders, the effective support length (the distance between two support points) is 32 m. The ambient temperature around the bridges in this line ranges from 2 °C ~ 36 °C

1.3. Track geometry inspection data

The track inspection car utilizes the Inertial-Reference method [58–60]. A detailed introduction of track geometries can be found in [58–66]. As illustrated in Fig. 3, the track longitudinal profile is obtained by combining carbody-wheel relative distance and double integration of carbody acceleration, which is followed by a HIGH pass filtering process to eliminate trend drift. It has been proven numerically and experimentally that the effective wavelength range is from 1 m to 120 m (for some inspection cars, the maximal wavelength can be up to 200 m). The measured track longitudinal profile can be understood as the dynamic displacement of the wheel along the rail line. The final measurement results are integrated with track geometry and stochastic irregularities, base deformation (e.g. bridge deflection and camber, subgrade settlement and etc.), and condition of the inspection train itself (e.g. wheel polygonal irregularities).

To monitor the bridge deformation based on track geometry inspection data over the long term, an accurate and reliable position information of the geometry inspection data is a prerequisite in this study. However, due to various issues regarding train's positioning system, such as degraded adhesive conditions between rail and wheel, sensor failures and poor GPS signal, the positions of multiple runs of track geometry inspections are far from consistent. Sometimes, the milepost error of

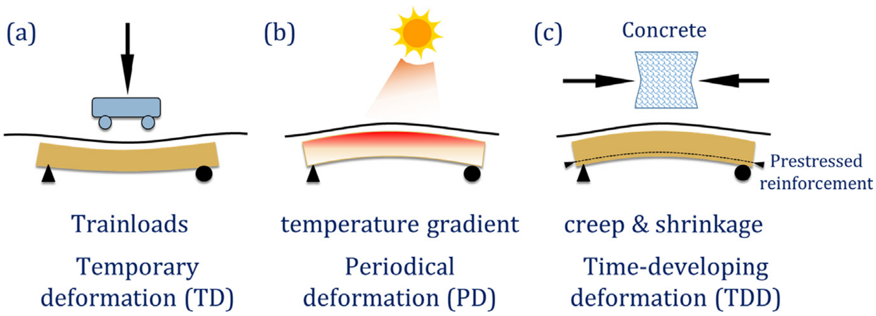

Fig. 1. Three major extrinsic factors that lead to bridge deflection or camber, including dynamic trainload, vertical temperature gradient, and creep & shrinkage of concrete.

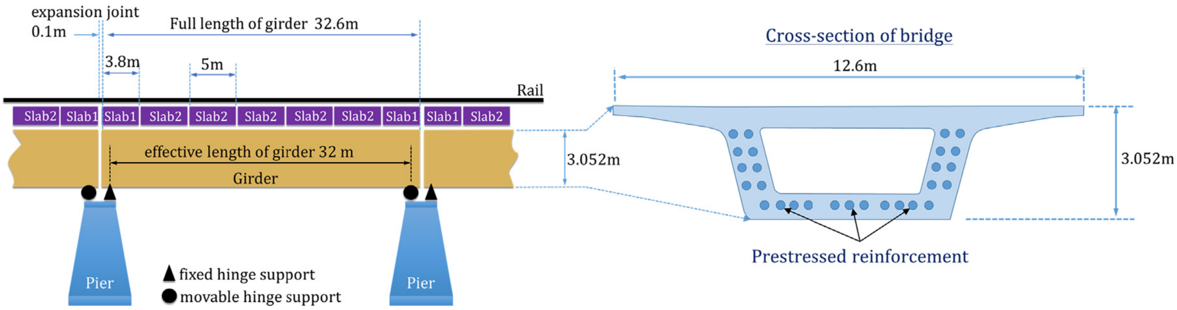

Fig. 2. The layout of CRTS I slab track on the 32 m simply supported beam. (Full section pre-stress).

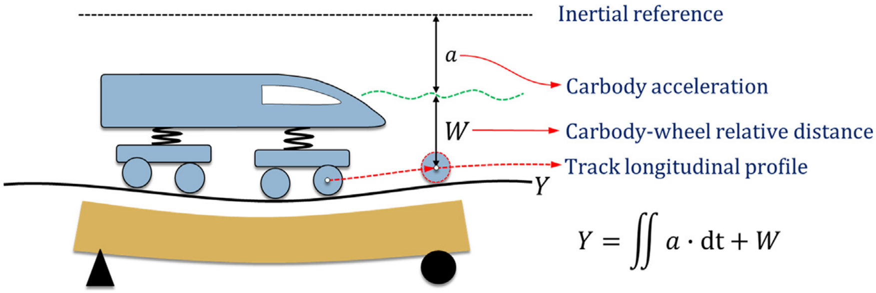

Fig. 3. The measurement principle of track longitudinal profile using the Inertial-Reference method. Here variable Y refers to the measured track longitudinal profile, a and W refer to carbody acceleration and relative distance between carbody and wheel, respectively.

between two inspection runs can even reach hundreds of meters, which needs to be aligned and synchronized to the same spatial coordinate. This is referred to as "position synchronization", a long-standing important research problem in the area of track data analytics. In our previous research, we have proposed a novel approach to more accurately and expediently synchronize track geometry inspection positions via big-data fusion [67]. In this paper, the dataset has been processed by the model proposed in [67], where the relative milepost error is less than 0.3 m.

The track geometry measured by the track inspection car is treated as a stochastic process along the mileage-axis [66,68]. Along the time-axis, however, it is found that the track geometry waveform does not change randomly over time comparing different inspection runs after milepost synchronization. Fig. 4 illustrates the comparison of rail longitudinal profile between four inspection runs. In particular, for the bridge-based section, an obvious periodic change (with a periodic interval of 32 m) of the waveform along the mileage axis can be observed, which cannot be seen in the subgrade-based section. Additionally, the bridge-based section also shows a greater difference between different inspection runs compared to the subgrade-based section. It is the waveform differences between different inspection runs and different spans of bridge that are the key to revealing the characteristics of bridge deformation. Although this difference is small and features a significant variance and uncertainty, it turns out to be quite meaningful under statistical significance.

2. Literatures review and contribution of this paper

2.1. Temporary deformation (TD)

TD is determined by trainloads and bridge stiffness. Increasing of trainloads and degradation of stiffness will cause larger TD and the direction of TD is downward. There are a lot of publications regarding the interaction between bridges and trains, experimentally [4,9] and numerically [10–20,23].

As for bridge stiffness, Gonzales *at al.* (2013) [51] studied the stiffness properties of railway bridges between winter (temperature below 0 °C) and summer. It was found that low temperatures tend to increase the value of the mean and variance of the measured natural frequencies of a bridge. An interpretation of this change is hypothesized as due to changes in the stiffness parameters of some materials with the onset of frost. A conclusion can be drawn according to [51] that temperature will not influence bridge stiffness when the temperature is above 0 °C. A similar study based on natural frequency can be found by reference to [52].

Besides the frost caused by low temperatures, concrete cracking is another major factor leading to stiffness degradation by softening the stress–strain relation [69,70]. However, clues regarding stiffness degradation of high-speed railway bridges

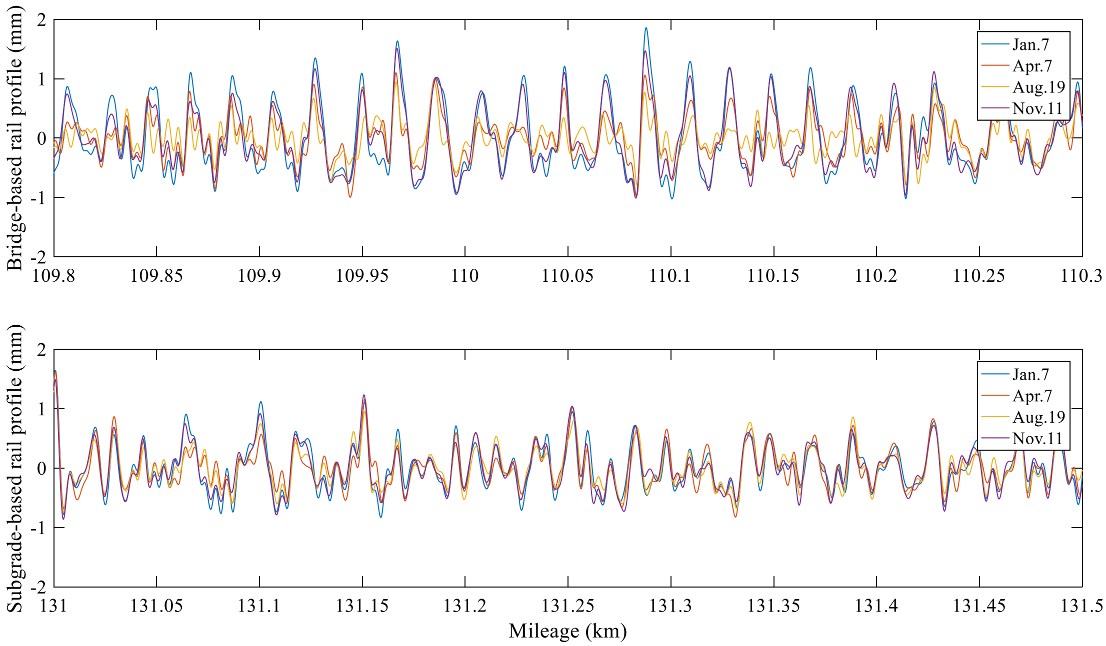

Fig. 4. Comparison of rail longitudinal profile between four inspection runs after mileage synchronization. (a) and (b) are the waveforms of the bridge-based and subgrade-based sections.

are rarely observed. Due to the durability of the design and the application of full section pre-stressing, it is almost impossible for cracks to be produced.

2.2. Periodical deformation (PD)

Though it is mentioned above that ambient temperature does not affect bridge stiffness when above 0 °C, thermal gradient does have a significant influence on bridge deformation due to thermal expansion and shrinkage of concrete [47–52].

In 2002, Carin L. *et al* [48] presented measurement data of thermal gradients through the depth of a segmental box girder bridge over 2.5 years. A strong seasonal periodical fluctuation of temperature differences as well as bridge deformation can be observed. Similar studies on the seasonal effects can be found in [50–52].

By reference to [48], the relationship between the temperature gradients and the middle span bridge deflection ω_c can be expressed as

$$\omega_c = \frac{Ml^2}{16EI} \tag{1}$$

$$M = \alpha E \cdot \int T(y)b(y)ydy \tag{2}$$

where, M is the equivalent bending moment caused by thermal effect, l is the effective span of a simply supported beam; I is the inertial moment of the bridge cross section and E is the modulus of elasticity. $T(y)$ is the temperature difference at distance y from the centroid of a section; $b(y)$ is the width of section at distance y from the centroid; α is the coefficient of thermal expansion (11×10^{-6}/°C);

Fig. 5 presents a case of measured positive temperature gradients. The measured data is cited from [48]. Similar results can be found in [54] and [55].

It is reported by [46] that a fifth-order curve is a good model of the distribution of temperatures through the depth of a concrete superstructure. The equation is

$$T(y) = T_s \cdot \left(\frac{y}{y_c}\right)^5 \tag{3}$$

where, $T(y)$ is the temperature at a depth y below the top surface (°C); T_s is surface temperature (°C); y is the depth below the top surface (mm) and y_c is the depth of the coolest position (mm). In the case of [56], y_c is specified to 1200 mm.

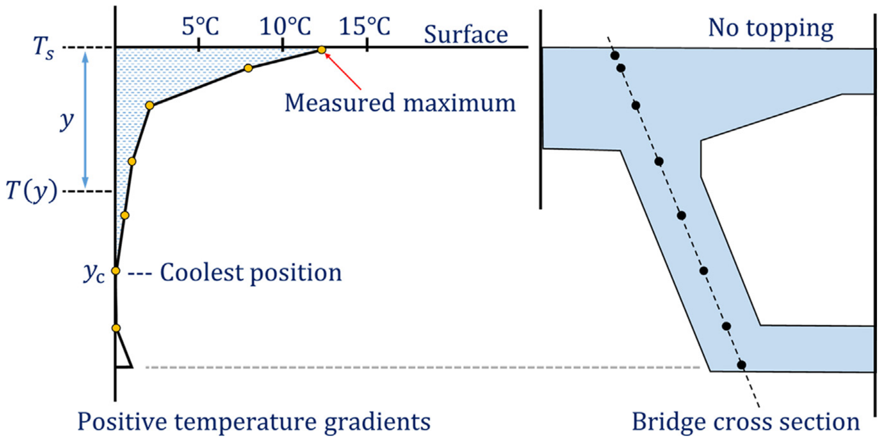

Fig. 5. Illustration of a case of positive temperature gradients.

In 1983, Potgieter and Gamble [57] presented equations to predict thermal gradients of concrete bridges considering ambient climatic conditions of solar radiation, daily ambient temperature variation, and wind speed. A case is given in [57] for San Antonio where the appropriate equations are as follows:

$$T_s(S, TV, v) = 28.2\left(\frac{S\alpha}{29.089} - 0.7\right) + 0.352(TV - 11.1) + F(v) \tag{4}$$

where, $F(v) = 32.3 - 4.84v + 0.771v^2 - 0.088v^3 + 0.00463v^4$ is the temperature influenced by wind speed v (m/s); S is the total daily solar radiation (KJ/m^2); TV is the ambient temperature variation (°C); α is the absorptivity (0.7 for plain concrete and 0.9 for asphalt). [57]

An accurate prediction of thermal gradients of concrete bridges is not easy since it requires varieties of ambient climatic conditions, which feature great uncertainty. It is recommended for readers to refer to [49] for a deeper understanding concerning thermal gradients of concrete bridges.

2.3. Time-developing deformation (TDD)

It has long been observed that railway bridges (mainly simply supported pre-stressed bridges) tend to deform upward like a camber gradually as time passes [24–36,40–41]. Here the upward change trend is in the scope of TDD. There are multiple factors that contribute to TDD, including prestress losses and the creep and shrinkage of concrete. The latter, creep and shrinkage of concrete, is thought to be the dominant factor leading to TDD. Creep and shrinkage of concrete under pressure is a natural process. There are numerous studies regarding the evolution of creep in different situation and it is reported that concrete creep and shrinkage are influenced by many factors, including relative humidity, temperature under load, size effect, water to cementitious ratio, age at loading, stress-strength ratio at loading and others. [23,31,34,36,37,46].

Wenjun He [36] deeply researched the long-term camber of pre-stressed bridges caused by creep and shrinkage of High Performance Concrete (HPC). Some real measured results of the camber of pre-stressed bridges are provided within a one-year period in [36], but the time sampling was too short to reveal the evolution of bridge camber over the long term.

There are a lot of variations for bridges in the field environment. The temperature and humidity change irregularly compared to the laboratory environment. The complex environment also leads to the problem that the results from a single bridge span do not convince without statistical significance. Thus, the major difficulty for studies to be carried out is the lack of field data regarding the deformation of bridges. Moreover, it is uneconomical and almost impossible to install monitoring systems on a number of bridges. The installation of monitoring systems is costly and more likely to be used to monitor bridges with special structures or large spans, such as suspension bridges and cable-stayed bridges. Since real observations are not easy to obtain, empirical models were proposed to predict the long-term camber of pre-stressed bridge girders, such work can be found in [24–26].

2.4. Intended contributions of this paper

This paper proposes a low-cost, data-driven approach to assess and predict bridge deformation using track inspection big data. Track inspection has been primarily used for assessing track conditions. However, due to the bridge-track-vehicle interaction, this data source may provide additional insight into the condition of the bridge. Using track inspection data to approximately evaluate bridge conditions has not been attempted in prior literature. If successful, this method can provide a secondary use for the enormous amount of track inspection data that was not fully utilized for this purpose before.

The main contributions of this paper are summarized in the following points:

- A Bridge Deformation Assessment model (BDA-model) with a sophisticated signal processing process is introduced to manipulate track geometry inspection data for the extraction of bridge-related components;
- A Bridge Dynamical Deformation index (BDD index) is defined to quantify bridge deformation based on track geometry inspection data;
- The Temperature-Time-Deformation model (TTD-model) is established to describe bridge deformation with respect to ambient temperature and length of service of the bridge. Three types of TTD equations are proposed, including exponential-, hyperbolic- and linear-TTD equations.
- A track geometry inspection dataset over 2.6 years with 563 bridge spans is applied as a case study. A prediction of the increase of the BDD index over the following 3 years is given with a 95% confidence level;
- A further discussion is presented regarding model uncertainty and application prospects.

3. Data processing and model framework

The data processing and model framework are illustrated in Fig. 6. There are three parts:

A: **Dataset Loading and preprocessing**. There are two main data sources, including track geometry inspection data and historical ambient temperature corresponding to the inspection runs. The track geometry inspection data should undergo the mileage synchronization procedure (please refer to [67]) to ensure the relative position error (RPE) is less than 0.3 m, so that the multiple runs of geometry data can be used to monitor bridge deformation in the long term.

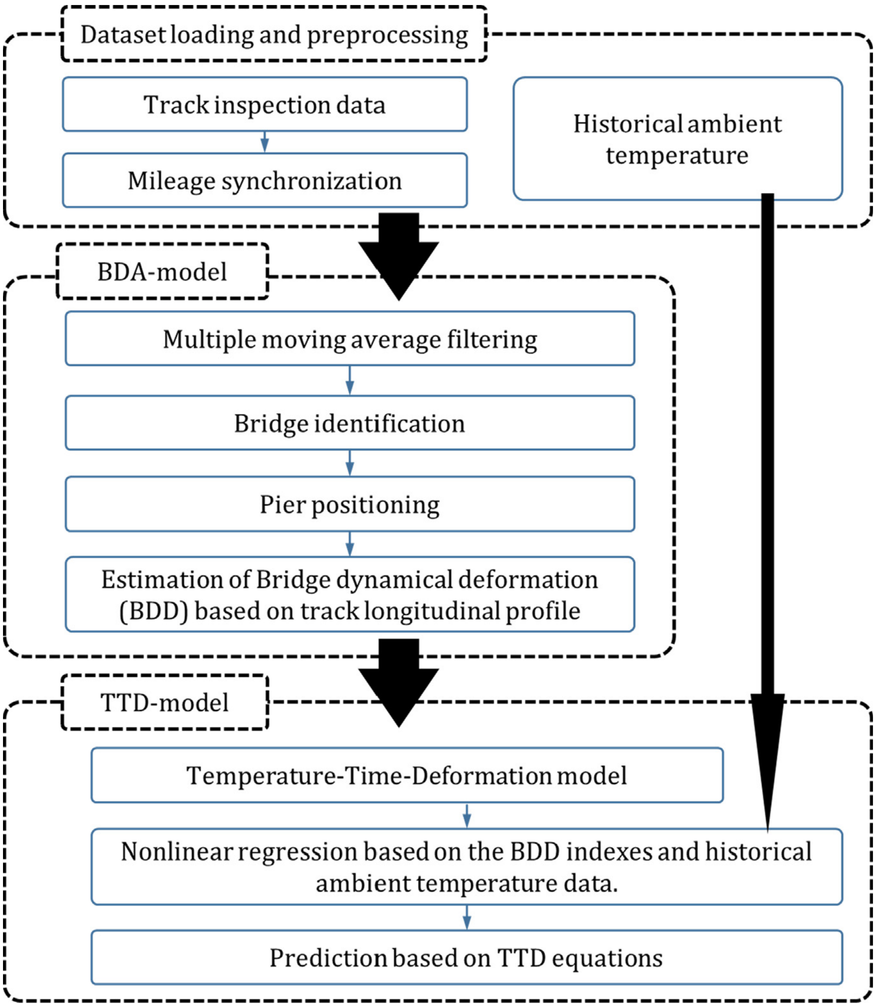

Fig. 6. Data processing flow chart.

B: **Bridge Deformation Assessment model** (BDA-model). This part consists of a sequence of data processing operations. A multiple moving average filtering method is applied, based on which peaks and valleys are extracted for bridge span estimation and pier positioning. Furthermore, the bridge dynamic deformation (BDD) is defined as a feature of bridge deformation. A method to estimate BDD based on rail longitudinal profile is proposed.

C: **Temperature-Time-Deformation model** (TTD-model). This part presents a model to separate the temperature-related and concrete-creep-related components that lead to bridge deformation in the field environment. Three types of TTD equations, Exponential-, Hyperbolic-TTD and Linear-TTD equations, are proposed and parameters are estimated. Finally, a prediction is given on the increase of bridge deformation in the following ten years.

4. Bridge deformation assessment model

4.1. Multiple moving average filtering (MMA filtering)

Since the bridge-related deformation waveform is covered up by the stochastic track geometry irregularities, a filtering process is necessary to recognize the bridge span and to separate the bridge-based rail profile waveforms of each bridge span. A direct way to reduce random disturbance is by taking the average of multiple measurements. The filtering method used in this section is **multiple moving average (MMA) filtering**, the most common filtering method used in engineering field. There are two parameters of MMA filtering: the number of points for the single average operation N and the number of times for average operations M. MMA filtering is equivalent to Gaussian filtering.

The purpose of filtering is not frequency truncation, but to reduce the random disturbance of the rail profile. More importantly, the filtered results should be as smooth as expected so they can be used for the recognition of bridge piers by estimating the peaks and valleys in Section 4.2. Mathematically, the peak and valley of a digital signal$\boldsymbol{y} = \{y_i | i = 1, 2 \cdots, n\}$ is defined as Eqn. 5:

$$\mathrm{typeof}\, y_i = \begin{cases} peak, & y_i > y_{i-1} and y_i > y_{i+1} \\ valley, & y_i < y_{i-1} and y_i < y_{i+1} \,; i = 2, \cdots, n-1 \\ notpeakor\, valley, & otherwise \end{cases} \tag{5}$$

The appropriate values of the parameters (N and M) are essential to the performance of the filtered results. If the values of N and M are too small, they will leave too many peaks and valleys on the filtered curve, while values that are too large will excessively smooth the waveform. The "appropriate values" of N and M mentioned here are aimed at bridges with a span of 32 m. There are other appropriate values for N and M relevant to infrastructure with other periodic lengths, such as a subgrade with a 20 m periodic structure.

Through multiple numerical tests, the appropriate values for N and M used in this section are set at N = 20 and M = 20. The sampling interval of the inspection car is 0.25 m, so it indicates the moving average filtering is taken on every 5 m (20points $\times$ 0.25m) length of rail, and the filtering is processed 20 times. The filtering performance is presented in Fig. 7. As shown, the original waveform contains a lot of random fluctuations, and there are many irregular peaks and valleys. As a comparison, the filtered result (the black curve) becomes much smoother. The peaks (red circles) and valleys (red plus symbol) of the filtered curve are distributed regularly on the bridge-based section.

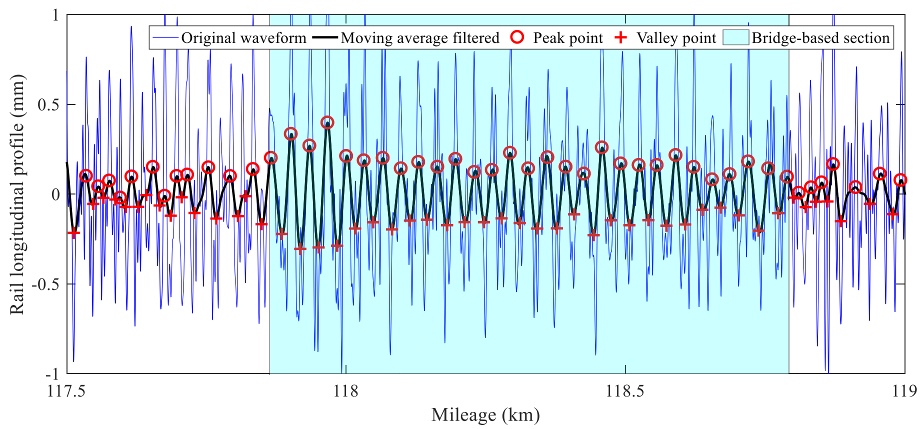

Fig. 7. Bridge span estimation based on peaks and valleys of the filtered waveform. The range with cyan background represents the bridge-based section.

4.2. Bridge span identification

This section deals with the recognition of the bridge span. The following contexts are based on two possible but opposite **hypotheses**:

- H_0- the piers are located at the peaks;
- $H_1-$the piers are located at the valleys.

There follows an essential question: which hypothesis should be accepted, or should both of them be rejected? When both H_0 and H_1 are rejected, it indicates the piers are not located at the peaks or valleys, and the models presented in the coming sections become invalid. This question is of great importance and it is addressed in Section 4.3 in particular. This section retains both hypotheses and the related models are provided separately.

The positions of peaks and valleys of the filtered results are denoted as $\boldsymbol{p} = \{p_i | i = 1, 2 \cdots, s\}$ and $\boldsymbol{v} = \{v_i | i = 1, 2 \cdots, t\}$, respectively. Then, the bridge middle span position and bridge span, denoted as a value pair $(\boldsymbol{m}, \boldsymbol{l})_k = \{(m_i, l_i) | i = 1, 2 \cdots, s-1, k = p\, or\, v\}$ are estimated based on vector$\boldsymbol{p}$ and $\boldsymbol{v}$ according to Eqn. 6

$$\begin{cases} (m_i, l_i)_p = \left(\frac{p_{i+1}+p_i}{2}, p_{i+1} - p_i\right); i = 1, \cdots, s-1 \\ (m_i, l_i)_v = \left(\frac{v_{i+1}+v_i}{2}, v_{i+1} - v_i\right); i = 1, \cdots, t-1 \end{cases} \tag{6}$$

where, the subscripts p and v represent the estimation based on peaks and valleys, respectively.

The model is applied to the dataset introduced in Section 1.3 and the estimated bridge middle span position and bridge span are presented in Fig. 8. Fig. 8(a) shows that the MMA filtering process has a significant suppression effect on the waveform amplitude of the non-bridge-based rail section, while at the same time it maintains the characteristics of the bridge-based section. Moreover, it can be observed from Fig. 8(b) that the estimated bridge spans are concentrated around 32 m for the bridge-based rail section, compared to the disordered distribution of non-bridge-based section, which can also be observed from the distribution histogram presented in Fig. 8(c).

To further address the bridge span identification mathematically, a normal distribution fitting of peak-based and valley-based bridge span is carried out, and we get $l\ N(32.781, 1.427)$, the fitting result is illustrated in Fig. 9. Here the mean value is 32.781, close to the real length of one period of bridge structure (32.7 m), with only a 2.48% error. At a 99% confidence level, we obtain a confidence interval of bridge recognition according to the estimated span of [29.11 m, 36.46 m].

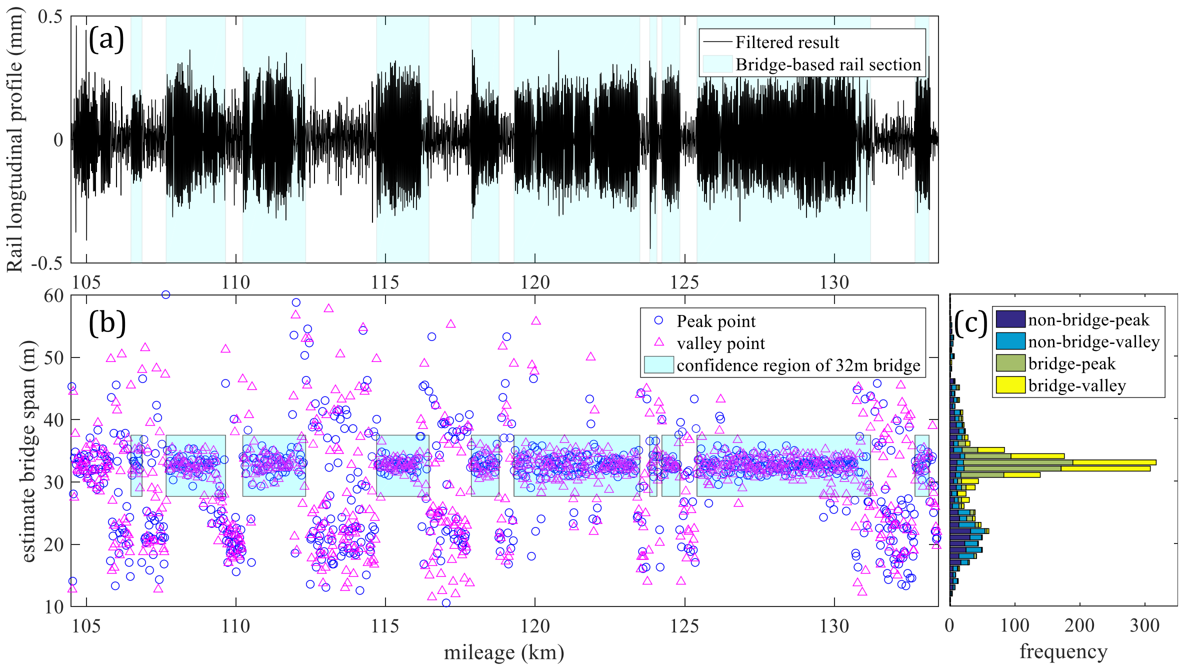

Fig. 8. Bridge middle span position and bridge span estimation. (a) shows the filtered results; (b) presents the estimation of $(\boldsymbol{m}, \boldsymbol{l})_k$ based on peaks and valleys according to the filtered results, with the cyan ranges representing the bridge-based track section; (c) is the distribution histogram of the estimated $(\boldsymbol{m}, \boldsymbol{l})_k$ in four categories, including non-bridge-based peaks, non-bridge-based valleys, bridge-based peaks and bridge-based valleys.

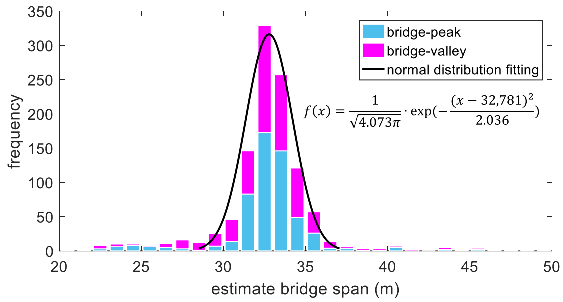

Fig. 9. Normal distribution fitting of peak-based and valley-based bridge span.

It should be mentioned that the distribution fitting is based on results of both peaks and valleys, because as long as we do not reject both H_0 and H_1, the peaks (or valleys) may be corresponding to piers and the valleys (or peaks) to be the middle span. In both conditions, $(m_i, l_i)_p$ and $(m_i, l_i)_v$ can be used for the estimation of length of bridge span.

4.3. Pier position hypothesis validation

This section deals with the validation of the pier position hypothesis. First of all, a basic conclusion from material mechanics should be addressed. For simply supported beams, the equation of the deflection curve under loads is similar to a parabola with zero values at the two hinge supports. The two hypotheses can be validated by comparing the waveform of the rail longitudinal profile over one bridge span. The true hypothesis between H_0 and H_1 should better fit a parabola.

Let $(\boldsymbol{x}, \boldsymbol{y}) = \{(x_i, y_i) | i = 0, \cdots, 128\}$ be a sample of rail longitudinal profile data within one bridge span, in which the pier positions are specified according to H_0 or H_1. And $x_i = 32/128 \times (i-1)$ and y_i is the original rail longitudinal profile at position x_i.

A **standardization** of $(\boldsymbol{x}, \boldsymbol{y})$ is necessary considering that the stiffness of the bridge pier is great enough that it deforms much less than the girders. Thus, the magnitudes of rail longitudinal profile at the position of the piers are set to zero by subtracting a linear trend between the two piers. Then, we get a standardized $(\boldsymbol{x}, \widehat{\boldsymbol{y}}) = \{(x_i, \widehat{y}_i) | i = 0, \cdots, 128\}$ and we have Eqn. 7

$$\widehat{y}_i = y_i - \frac{1}{128}(i \cdot y_{128} + (128 - i) \cdot y_0); i = 0, \cdots, 128 \tag{7}$$

To observe bridge deformation from rail longitudinal profile over one single bridge span is difficult since the bridge deformation is almost covered up by the track geometry irregularity with random disturbances. However, by taking the average of $(\boldsymbol{x}, \boldsymbol{y})$ over multiple bridge spans, the common characteristics can be revealed. Fig. 10 illustrates a comparison of the average of rail longitudinal profile over multiple bridge spans based on the two hypotheses.

It is obvious that Fig. 10(a) is a more reasonable deflection of the bridge and there should not be a sharp angle at the middle span as in Fig. 10(b). Mathematically, the judgment of the pier position hypothesis can be described as Eqn. 8:

$$\begin{cases} V_0 = \min\limits_{k,b} \|\boldsymbol{\theta}_0 - k\boldsymbol{x} + b\| \\ V_1 = \min\limits_{k,b} \|\boldsymbol{\theta}_1 - k\boldsymbol{x} + b\| \end{cases} \tag{8}$$

where, $\boldsymbol{\theta}_0$ and $\boldsymbol{\theta}_1$ are the first order change rate of the average of $\boldsymbol{y}$ based on H_0 and H_1, respectively. k and b are linear fitting parameters. V_0 and V_1 are values representing the degree of linear approximation of $\boldsymbol{\theta}_0$ and $\boldsymbol{\theta}_1$. The valid hypothesis between H_0 and H_1 can be determined as the one with the smaller value of V_0 and V_1. Additionally, when both V_0 and V_1 are too large, it indicates both $\boldsymbol{\theta}_0$ and $\boldsymbol{\theta}_1$ are not similar to a linear function. Thus, a threshold for V_0 and V_1 is necessary to distinguish the abnormal situation. The validation process is written as Eqn. 9:

$$\text{pierpositionhypothesis} = \begin{cases} H_0, & V_0 < V_1 \text{and} V_0 < T \\ H_1, & V_0 > V_1 \text{and} V_1 < T \\ \text{rejectboth}, & otherwise \end{cases} \tag{9}$$

where, T is a threshold which is determined empirically. Here when $V_0 = V_1$ or both V_0 and V_1 are larger than T, both H_0 and H_1 are rejected, which can be interpreted as no bridge span of 32 m being detected.

It should be noted that there is no absolute result for the validation of H_0 and H_1. A comparison is necessary since sometimes H_0 is true and sometimes the opposite. In general, when the bridge is newly built and the environmental temperature is low, the bridge deforms downwards and H_0 is true. On the contrary, when the bridge has been in service for a long time and the environmental temperature is high, the bridge deforms upwards like a camber and H_1 is true. Fig. 11 illustrates the waveform comparison of rail longitudinal profiles on the same bridge span over 2.6 years. Though it is not clear for the peri-

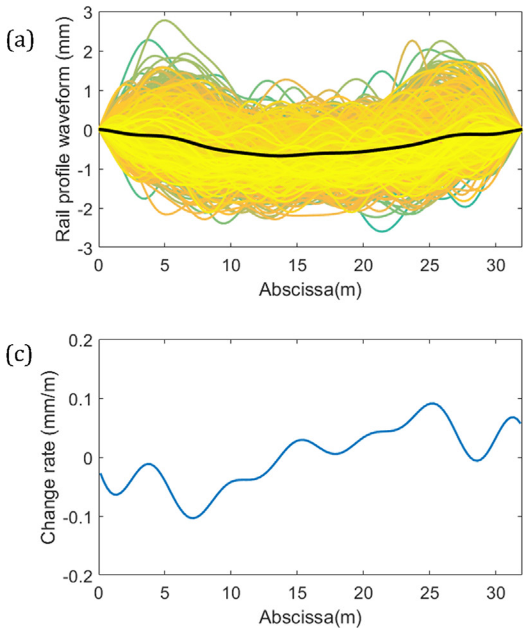

Fig. 10. Comparison between two different hypotheses regarding pier identification. (a) and (b) are rail longitudinal profiles of 563 spans based on H_0 and H_1, respectively; (c) and (d) are the first order change rates of the black curve in (a) and (b), respectively.

odic change, an overall increasing trend is obvious. In the early stage, the bridge bends downwards (see the blue curves). As time goes by, the downward trend of the waveform gradually decreases and an upward trend is shown (see the yellow curves).

4.4. Bridge dynamic deformation (BDD)

An index is introduced in this section to characterize bridge deformation. Compared to static bridge deformation, Bridge Dynamic Deformation (BDD) is proposed to describe the deformation of bridges serving in a field environment when trains cross the span. BDD is a final outcome influenced by multiple causes, including loads, bridge stiffness, environmental temperature, the development of concrete creep and shrinkage, and others. The following context describes how the BDD index is defined in this paper.

As is mentioned in Section 3.2, the rail longitudinal profile over a 32 m bridge span is standardized so that the offsets at the two hinge supports are set to zero by subtracting a linear trend. Thus, $y(x=0) = y(x=32) = 0$. Then, the BDD curve is defined with the form of Eqn. 10

$$y(x) = a \cdot x(x - 32) \tag{10}$$

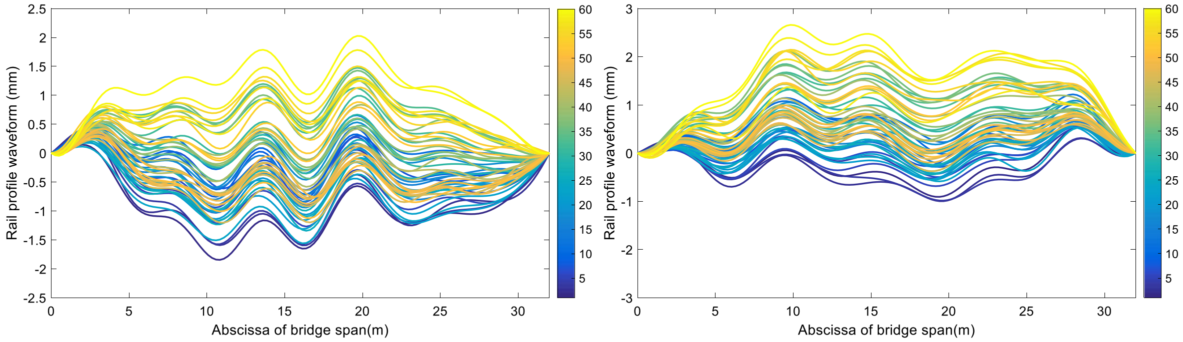

Fig. 11. The waveform comparison of rail longitudinal profile on the same bridge from January 2015 to August 2017 (the colors correspond to the time when the rail inspection was carried out). There are 60 inspection runs presented.

where a is the only parameter describing the amplitude of bridge deformation. When $a < 0$ or $a > 0$ the bridge deforms upwards or downwards, respectively. Also, $a = 0$ indicates the upward and downward trends of bridge deformation counteracting each other.

For a standardized rail longitudinal profile data sample over a 32 m bridge span, $(\boldsymbol{x}, \boldsymbol{y}) = \{(x_i, y_i) | i = 0, \cdots, 128\}$, the parameter a can be estimated based on the following least square model Eqn. 11:

$$\arg\min_a \frac{1}{2} \|\boldsymbol{y} - a \cdot \boldsymbol{x}^2 + 32a \cdot \boldsymbol{x}\|^2 \tag{11}$$

There are 129 pairs of data because the sampling interval of the track inspection car is 0.25 m and the effective length of the bridge is 32 m. The model is a standard convex optimization problem, and the result can be expressed as Eqn. 12

$$a = \left(\sum_{i=0}^{128} y_i\right) / \left(\sum_{i=0}^{128} x_i(x_i - 32)\right) = \frac{-1}{21844} \cdot \sum_{i=0}^{128} y_i \tag{12}$$

In this paper, instead of using a whole curve to describe the BDD, the middle span deformation is chosen as a feature since it is known that the maximum bridge deflection is reached when the train is at the middle span. Thus, the BDD index in this paper is defined as the offset between the quadratic fitting curve and the static reference at the middle span, as Eqn. 13, which is illustrated in Fig. 12.

$$BDD \triangleq 0 - y(x = 16) = \frac{16^2}{21844} \cdot \sum_{i=0}^{128} y_i = 0.0117 \cdot \sum_{i=0}^{128} y_i \tag{13}$$

The unit of the BDD index is millimeters. The definition indicates the direction of the BDD is upward. When a bridge deflects downward the value of BDD is negative, and vice versa.

With the definition above, the estimated BDD indexes of 563 bridges from January 2015 to August 2017 are calculated and presented in Fig. 13. As is shown, a seasonal periodic fluctuation with a general increasing trend can be observed. For each group in Fig. 13, the box-plot refers to 563 BDD indexes. The median, average and standard deviation of each group are given in Table A3 in Appendix.

5. Temperature-time-deformation model

This section focuses on the major constituent components of BDD. The Temperature-Time-Deformation model (TTD-model) is established and parameters are estimated based on the outputs from the BDA-model.

5.1. Components of BDD

Recalling that there are three major extrinsic factors in terms of bridge deformation which were listed in Section 1.2: trainloads, temperature gradient and creep and shrinkage of concrete over time. Thus, the BDD can be treated as a combined effect of the three components. According to **BDD superposition assumption** in Table A2, the function of the BDD index against dynamic trainload F, ambient temperature T and time t can be written in the following form Eqn. 14:

$$Y(F, T, t) = -\alpha(F) + \beta(T) + \gamma(t) \tag{14}$$

where, $\alpha(F)$, $\beta(T)$ and $\gamma(t)$ are the sub-functions of the BDD index with respect to F, T and t, respectively.

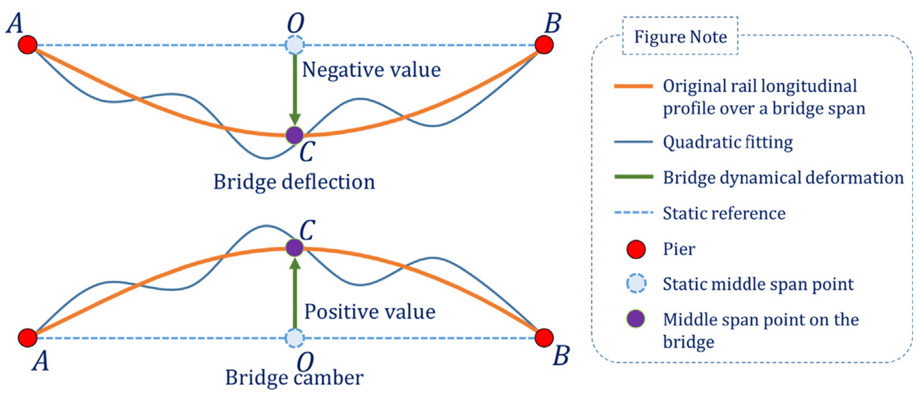

Fig. 12. Definition of Bridge Dynamic Deformation (BDD), the middle span offset between the quadratic fitting curve and the static reference.

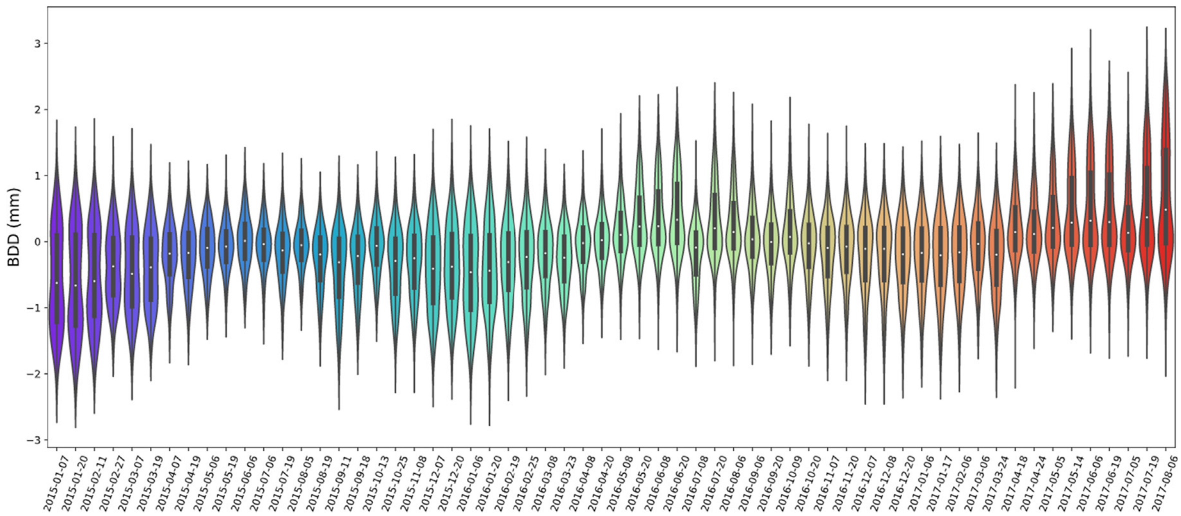

Fig. 13. The BDD indexes of 563 bridges from Jan. 7, 2015 to Aug. 8, 2017 (60 track inspection runs). The red plus symbols represent outliers.

5.2. BDD from the TD component

$\alpha(F)$ represents the bridge deflection caused by a dynamic trainload F. The direction of BDD caused by the trainload is downward, so there is a negative sign in front of $\alpha(F)$. According to the **TD assumption in** Table A2**: the load *F* can be taken as a constant**; we obtain Eqn. 15

$$\alpha(F) = A \tag{15}$$

5.3. BDD from the PD component

$\beta(T)$ represents the bridge deformation caused by temperature T. It should be noted that it is the temperature gradient of the girder in the vertical direction that matters, rather than the ambient temperature. According to Eqs. (1) to (3), we find that the middle-span deformation due to the temperature gradient is proportional to the temperature on the surface T_s. According to Eq. (4), T_s is determined by solar radiation, daily ambient temperature variation, and wind speed. Nevertheless, instead of estimating the surface temperature T_s, this paper proposes a simplified approximation by using the ambient temperature to address the temperature effect. According to the **PD assumption in** Table A2**, the BDD index is approximately proportional to the ambient temperature in long-term observation**. For a given reference temperature T_0, when $T > T_0$, there is a positive temperature gradient that makes the bridge bend upwards, and vice versa. When the ambient temperature happens to be T_0, the bridge is not influenced by temperature gradient, which means $\beta(T = T_0) = 0$. Then $\beta(T)$ is proportional to $T - T_0$; we obtain Eqn. 16

$$\beta(T) = B \cdot (T - T_0) \tag{16}$$

The coefficient B, with a unit of mm/°C, is an important parameter which reveals the relationship between bridge deformation and ambient temperature. It should be noted that the expression of $\beta(T)$ may be a debatable point. However, it can be understood as a linear approximation of the complicated influence of ambient temperature. Since the real temperature gradient of the bridge is too difficult to measure, the ambient temperature is an alternative and approximate choice.

5.4. BDD from the TDD component

$\gamma(t)$ represents the bridge deformation caused by the development of concrete creep and shrinkage. In the field environment, the situation is so complicated that temperature, humidity and trainloads change periodically with great uncertainty, which makes the development of concrete creep and shrinkage hard to measure by equipment or predict by empirical formulas. Instead, this paper provides a macroscopic description of the bridge deformation caused by creep-shrinkage through the development of the BDD index, without further consideration of the mechanism of concrete creep and shrinkage. According to the **TDD assumption** in Table A2, we get $\gamma(t = 0) = 0$ and $\gamma(t \to \infty) = \text{constant}$.

Combining with reference [36–37], where exponential and hyperbolic functions are used to describe the development of concrete creep and shrinkage, we suggest $\gamma(t)$ be described with three possible expressions: an exponential function $\gamma_e(t)$, hyperbolic function $\gamma_h(t)$ and local linear function $\gamma(t)$, as Eq. (17) to (19).

$$\gamma_e(t) = C \cdot \left(1 - e^{-\lambda t}\right) \tag{17}$$

$$\gamma_h(t) = D \cdot \frac{t}{E + t} \tag{18}$$

$$\gamma_l(t) = K \cdot t \tag{19}$$

The parameters of these three models can be interpreted by associating with the evolution process of bridge deformation due to concrete creep and shrinkage. The units of C and D are mm, and represent the limit of bridge deformation caused by creep-shrinkage. The units of λ and E are 1/day and day, respectively. The parameter λ is the exponential convergence rate. E is a parameter controlling the shape of the function $\gamma_h(t)$. The unit of K is mm/day, and it is a parameter valid in a local scope, but it holds the most intuitive meaning for the development speed of bridge deformation.

In brief, since $\alpha(F)$ is a constant, the TTD-model is independent of trainload F. The TTD-model can be written as three forms

$$Y_e(T, t) = -A + B \cdot (T - T_0) + C \cdot \left(1 - e^{-\lambda t}\right) \tag{20}$$

$$Y_h(T, t) = -A + B \cdot (T - T_0) + D \cdot \frac{t}{E + t} \tag{21}$$

$$Y_l(T, t) = -A + B \cdot (T - T_0) + K \cdot t \tag{22}$$

where, T represents temperature (°C) and t represents time (day). Eq. (20), (21) and (22) are named the E-TTD equation, H-TTD equation and L-TTD equation, respectively.

6. Model fitting and prediction

6.1. Nonlinear regression of the TTD equations

This section presents the results of parameter estimation of $Y_e(T, t)$, $Y_h(T, t)$ and $Y_l(T, t)$. The original data used to perform the fitting comes from ambient temperature data and the estimated BDD indexes as well as the corresponding track geometry inspection data, which are also provided in Appendix. By using the MATLAB toolbox *cftool*, Eq. (20) to (22) are fitted and results are presented as Eqns. 23, 24 and 25.

$$Y_e(T, t) = -1.85 + 2.07 \times 10^{-2} \cdot T + 25.61 \cdot \left(1 - e^{-2.237 \times 10^{-5} \cdot t}\right) \tag{23}$$

$$Y_h(T, t) = -1.94 + 2.02 \times 10^{-2} \cdot T + 20 \cdot \frac{t}{3.096 \times 10^4 + t} \tag{24}$$

$$Y_l(T, t) = -1.85 + 2.04 \times 10^{-2} \cdot T + 5.587 \times 10^{-4} \cdot t \tag{25}$$

where, the temperature data used for the fitting is the highest temperature of that day. The BDD indexes used are the mean values. The goodness of fit as well as the parameters A, B, C, D, E, T_0, λ and K are given in Table 1. Since the fitting data is not able to distinguish A and T_0, the value of $A + B \cdot T_0$ is given. Comparing with the results presented in Table 1, the following conclusions can be drawn:

- All three fittings share similar accuracy according to the goodness of fit;

Table 1
The estimation of parameters for E-, H- and L-TTD equations, including A, B, C, D, E, T_0, λ and K. The physical meaning of each parameter is given in Section 5.

Fitting type	Goodness of fit R^2	Parameter	Value	95% confidence bounds
Ftabl E-TTD (Y_e)	0.8793	B	0.0207	[0.0177, 0.0237]
		$A + B \cdot T_0$	1.85	[−1337, 1385]
		C	25.61	[−1385, 1334]
		λ	2.237e−5	[−1.23e−3, 1.27e−3]
H-TTD (Y_h)	0.8772	B	0.0202	[0.0172, 0.0233]
		$A + B \cdot T_0$	1.94	[−0.1328, 4.013]
		D	20	[−358.2, 398.2]
		E	3.096e + 04	[−6.483e + 05, 7.102e + 05]
L-TTD (Y_l)	0.8766	B	0.0204	[0.0174, 0.0234]
		$A + B \cdot T_0$	1.851	[−2.052, −1.65]
		K	5.587e−4	[4.733e−4, 6.441e−4]

- The temperature coefficient B is about 2.04×10^{-2}mm/°C according to the three TTD equations;
- For the E-TTD equation, the limit value of creep-shrinkage-caused bridge deformation is about 25.6 mm, which is greater than that of H-TTD (20 mm).
- The parameter K of L-TTD indicates that an average of 0.2 mm/year (5.59×10^{-4} mm/day) of deformation (upward) increase is observed in these years.

It should be noted that the fitting parameters for E- and H-TTD are very sensitive, since the 95% confidence bounds of $A + B \cdot T_0$, C, D and E change across a large range, as highlighted with red in Table 1. We can conclude that even though the track inspection dataset used in this case contains 2.6 years of data, it is still not sufficient to describe the time-developing trend of the BDD index over decades or even centuries. Nevertheless, how the deformation of a bridge develops in the far future (e.g. several decades) seems not of urgent importance. And the TTD model can still be used for the prediction of BDD index in the coming years, as presented in Section 6.2.

6.2. Prediction for the following 3 years

A direct application of the fitted TTD equations is the prediction of TDD component in the future. The fitting performance of the three models are illustrated in Fig. 14. To avoid the disturbance of temperature effect, the results of TTD equations with temperature of 20 °C (simply as a reference) are also presented in Fig. 14. As shown in Fig. 14(a), the results of the three TTD equations almost coincide with each other within the time range from January 2015 to August 2017. However, when it comes to a long-term time scope, e.g. 5 years in Fig. 14(b), the curves of the three TTD equations disperse. The L-TTD equation shows a linear trend, and the E-TTD and H-TTD equations gradually deviate from L-TTD. In the long-term prediction (right), we assume there would be similar temperature fluctuation in the following years, so we can observe a gradually increasing trend, as well as the BDD fluctuation with respect to the changing temperatures.

The predicted amounts of increase of bridge deformation in 0.5 years, 1 year, 2 years and 3 years are given in Table 2, with the 95% confidence bounds in brackets. It is expected that the bridge deformation will increase by 0.5 mm in 2 years, and 0.7 mm in 3 years according to the three TTD models. The predicted amounts of the E- and H-TTD equations are a little bit smaller compared to the L-TTD equation. Additionally, the 95% confidence bounds of E- and H-TTD are much larger than L-TTD since the fitting parameters are much more sensitive for nonlinear regression (e.g. exponential and hyperbolic for E- and H-TTD in this case) than for linear regression (e.g. L-TTD). It can be explained at the same time with the large range of confidence bounds of each fitting parameter presented in Table 1.

7. Discussion

7.1. Model uncertainty

There are two main factors contributing to the prediction accuracy of the TTD model: (1) from model aspect: the selection of parameters in the TTD model and (2) from data aspect: the reliability of the dataset in use.

From model aspect, as mentioned in Section 2.2, PD is mainly caused by the cross-section thermal gradient, which is determined by ambient climatic conditions, such as solar radiation, daily ambient temperature variation, and wind speed. Additionally, Section 2.3 shows that TDD mainly depends on the development of concrete creep and shrinkage, which is influenced by many factors, including relative humidity, temperature, size effect, stress-strength ratio and age at loading and etc. However, in Section 5, only the two most important and general parameters are selected for modeling, that is the highest ambient temperature T and time t.

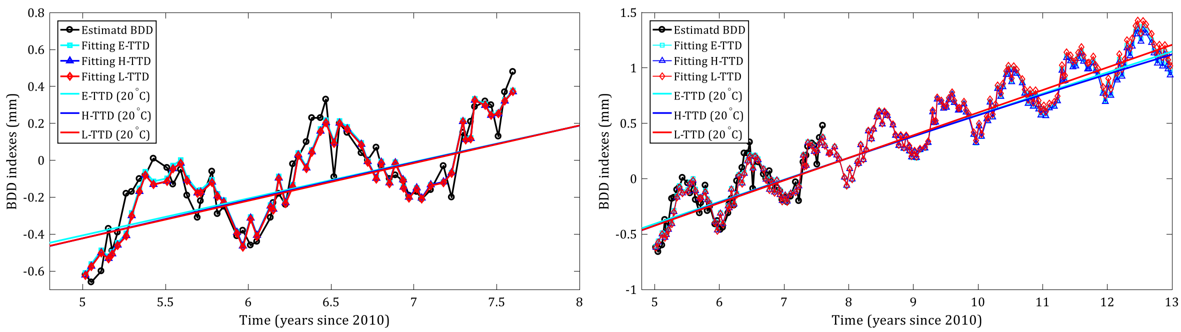

Fig. 14. The fitting performance of the three models. The short term (left) and the long-term (right) prediction of TDD according to the E-TTD, H-TTD and L-TTD equations. Note that in the long-term perdition (right), we assume there would be similar temperature fluctuation in the following years.

Table 2
The predicted amount of increase of deformation on the median value BDD indexes in the following 3 years. The value in brackets is the 95% confidence bounds.

Type of model	Amount of permanent bridge deformation increase (mm)			
	0.5 years later	1 year later	2 years later	3 years later
E-TTD	0.208 (−0.018, 0.433)	0.305 (0.017, 0.593)	0.499 (−0.004, 1.00)	0.692 (−0.132, 1.516)
H-TTD	0.207 (−0.019, 0.433)	0.305 (0.020, 0.590)	0.497 (0.010, 0.985)	0.686 (−0.096, 1.467)
L-TTD	0.209 (0.016, 0.401)	0.311 (0.113, 0.509)	0.515 (0.305, 0.726)	0.719 (0.491, 0.947)

From data aspect, four factors contribute to the prediction accuracy of the TTD model: (1) the ambient temperature is obtained from the weather reports of the nearest city along the rail line, it is not exactly the temperature on the bridge surface; (2) the temperature readouts are only accurate to 1°centigrade; (3) only the maximum and minimum ambient temperatures are provided and the exact temperatures when the inspection car is present are unknown; (4) the estimation of BDD index may be influenced by track slab and rail geometry, since the BDD are defined and calculated from track inspection dataset. The fitting performance and residual errors are illustrated in Fig. 15, with more detailed weather conditions on the day the track geometry inspection is carried out (the data is given in Table A3 in Appendix). It can be found that the general development trend of the fitting of BDD is consistent with the real estimated BDD indexes. At some times, the residual error even reaches 0.2 mm.

There is a significant decrease of the BDD index to be found on July 8, 2017, as highlighted in red. At the same time, the highest ambient temperature witnessed is relatively low compared to the two nearest inspection runs. Moreover, it is found that there was rain on July 8, 2017, and the sharp drop of the BDD can be explained by the reduction of the temperature gradient due to a cooling effect of the rain. Moreover, it should be noted that the weather condition can be quite complicate, since for a rainy day it could be a light rain or a heavy rainfall. Similarly, for a cloudy day, the cloud may lead to different solar radiation energy absorbed by the bridge, and the degree of how much cloud exists beyond the bridge is hard to be quantified. As a result, the exact weather conditions are the major but uncertain factor contributing to the residual fitting error.

7.2. Application prospects

Since the track geometry inspection data is easily accessible, the BDA model proposed in this paper can be applied to other rail lines and an assessment of bridge deformation can be carried out. Moreover, combining with the ambient climatic condition recorded by the National Weather Service, the TTD-model can be used to make a prediction on the development trend of bridge deformation in the following years. With the increasing amount of track geometry inspections year by year,

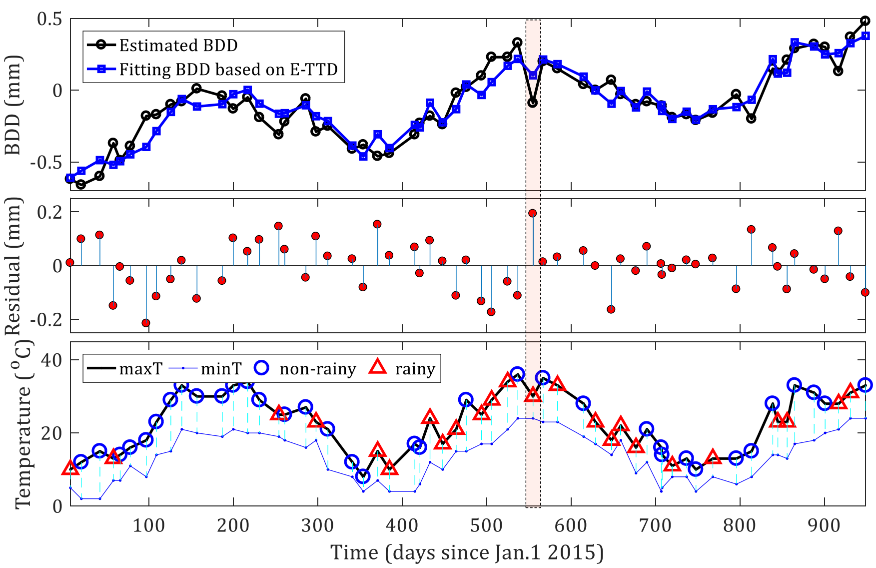

Fig. 15. Temperatures related to the track inspection runs. Different symbols represent different types of weather. The legends *maxT* and *minT* of Fig. 15(c) represent the maximal and minimal temperatures, respectively. See Table A3 in Appendix for details. The date of the highlighted data is July 8, 2017. Only the case of E-TTD is presented since the three fitting equations are similar to each other.

the fitting performance of TTD equations can be enhanced. The predictions can be tested and the TTD-model will be corrected and updated each time a new track geometry inspection is carried out.

It should be noted that the method proposed in this paper does not aim at estimating the deformation of one single bridge span, but towards a range of bridges which may contain hundreds of bridge spans. It is effective under statistical significance.

What's more, the methods and some conclusions given in this paper are of reference value for research topics on bridge condition evolution, rail geometry degradation and prediction-based infrastructure maintenance.

8. Conclusions

This paper proposed a novel approach to evaluate railway bridge deformation based on track geometry inspection big data, which is primarily used for assessing track conditions.

The Bridge Deformation Assessment model with a sophisticated signal processing process, including MMA filtering, peak and valley estimation and curve fitting, is proposed to manipulate track geometry inspection data for extracting bridge-related components. Then, a Bridge Dynamic Deformation (BDD) index is defined to quantify bridge deformation based on the extracted bridge-related waveforms. The Temperature-Time-Deformation (TTD) model is established to describe bridge deformation with respect to ambient temperature and length of service time. Three types of TTD equations are proposed, including exponential-, hyperbolic- and linear-TTD equations.

A track geometry inspection dataset over 2.6 years with 563 bridge spans is applied as a case study. It is found that the BDD index changes with ambient temperature by 0.02 mm/°C on average and increases with time by 0.2 mm/year during the 2.6-year period. Furthermore, a prediction of the amount of increase of the BDD index over the following 3 years is given with a 95% confidence level. It is expected that the BDD index will increase by 0.5 mm in 2 years, and 0.7 mm in 3 years according to the TTD model.

Finally, the model uncertainty is discussed from data aspect and model aspect, including the selection of parameters in the TTD model and the reliability of the dataset in use. It is found that the exact weather conditions are the major uncertain factor contributing to the residual fitting error. The methods and some conclusions given in this paper are of reference value for research topics on bridge condition evolution, rail geometry degradation and prediction-based infrastructure maintenance.

Declaration of Competing Interest

The authors declare that they have no known competing financial interests or personal relationships that could have appeared to influence the work reported in this paper.

Acknowledgements

The present work has been supported by the National Natural Science Foundation of China (52008198, 51425804, 51608459, 51808221 and 51378439), the United Fund for Key Projects of China's High-Speed Railway (U1334203 and U1234201), the China Postdoctoral Science Foundation (2020M682037) and Jiangxi Natural Science Foundation (20181BAB216029). The authors Yuan Wang (No. 201707000036) and Huiyue Tang (No. 201707000037) are financially supported by the China Scholarship Council CSC. Dr. Xiang Liu is funded by the US Federal Railroad Administration at the time of writing this paper. However, the authors are solely responsible for all views and analyses in this research.

Appendix

Table A1
Abbreviations and Assumptions.

Abbreviations	Explanation
TD	Temporary deformation of bridge
PD	Periodical deformation of bridge
TDD	Time-developing deformation of bridge
MMA	Multiple moving average filtering
BDD	bridge dynamical deformation index
BDA-model	Bridge deformation assessment model
TTD	Temperature-Time deformation model
E-TTD	TTD equation with exponential function component
H-TTD	TTD equation with hyperbolic function component
L-TTD	TTD equation with local linear function component

Table A2
Assumptions and rationales.

Assumptions	Explanation	Rationale
BDD waveform assumption (Section 4.1)	For simply supported beams, the deflection curve equation under loads is similar to a parabola with zero values at the two hinge supports. In this paper, quadratic parabolic equation is applied to fit the BDD waveform.	This assumption is based on common knowledge from mechanics of materials. A quadratic parabolic equation is applied to fit the BDD waveform for simplification. Since there is a lot of noise (random track irregularity) in the measured data, using a higher order parabolic equation may lead to over-fitting.
BDD superposition assumption (Section 5.1)	The three components of bridge deformation (TD, PD and TDD) are independent of each other, and the magnitude of bridge deformation from the three components is small and obeys the principle of superposition.	1) TD, PD and TDD are caused by different and independent factors. 2) The bridge deformations from TD, PD, and TDD are much smaller than the bridge span (32 m).
TD assumption (Section 5.2)	The dynamical load F can be taken as a constant.	The track inspection cars do not carry passengers, and the weight of the inspection car can be taken as a constant. The inspection speed is always the same when running on the same track section, so the dynamical load F can be taken as a constant.
PD assumption (Section 5.3)	Periodical BDD is approximately proportional to the ambient temperature for a complex field environment over long-term observation.	In fact, PD is related to multiple ambient climatic conditions, such as solar radiation, daily ambient temperature variation and wind speed. However, in complex field environments, the exact ambient variables change with a lot of uncertainty. A simple treatment is by a linear approximation and only considers the influence of ambient temperature. This assumption becomes invalid when the ambient temperature is below 0 °C because of the influence of frost [51].
TDD assumption (Section 5.4)	1) Initially there is no creep or shrinkage effect of concrete; 2) As time goes by, the creep and shrinkage effect will not increase infinitely.	Since TDD is mainly caused by creep and shrinkage of concrete, the evolvement of TDD over time is assumed to be similar to the condition evolution of concrete, which can be found in [24–36,40–41].

Table A3
Temperature and weather on the day the inspection data is obtained, with bridge dynamic deformation estimated from the inspection data.

Days from Jan.1 2010	Temperature and weather			Bridge dynamic deformation (BDD index) (mm)		
	maximum	minimum	weather	median	average	standard deviation
1831	10	5	rainy	−0.62	−0.56	0.77
1844	12	2	cloudy	−0.66	−0.61	0.81
1866	15	2	sunny	−0.60	−0.53	0.74
1882	13	7	rainy	−0.37	−0.37	0.56
1890	14	7	cloudy	−0.49	−0.45	0.65
1902	16	11	sunny	−0.39	−0.41	0.58
1921	18	8	cloudy	−0.18	−0.21	0.46
1933	23	14	cloudy	−0.17	−0.21	0.47
1950	29	15	cloudy	−0.10	−0.11	0.41
1963	33	21	cloudy	−0.08	−0.08	0.37
1981	30	20	cloudy	0.01	0.01	0.41
2011	30	19	cloudy	−0.04	−0.05	0.38
2024	33	21	cloudy	−0.13	−0.18	0.45
2041	34	20	cloudy	−0.05	−0.07	0.36
2055	29	20	sunny	−0.19	−0.27	0.46
2078	25	19	rainy	−0.31	−0.41	0.60
2085	25	18	sunny	−0.22	−0.29	0.49
2110	27	16	cloudy	−0.06	−0.08	0.41
2122	23	18	rainy	−0.29	−0.36	0.55
2136	21	10	cloudy	−0.25	−0.31	0.54
2165	12	8	sunny	−0.41	−0.43	0.65
2178	8	4	sunny	−0.38	−0.37	0.63
2195	15	7	rainy	−0.46	−0.47	0.71
2209	10	4	rainy	−0.44	−0.41	0.69
2239	17	4	cloudy	−0.31	−0.32	0.61
2245	16	6	cloudy	−0.23	−0.28	0.59
2257	24	12	rainy	−0.18	−0.21	0.49
2272	17	10	rainy	−0.24	−0.27	0.47
2288	21	15	rainy	−0.02	−0.05	0.41
2300	29	15	cloudy	0.02	0.02	0.41
2318	25	17	rainy	0.10	0.15	0.46
2330	29	17	rainy	0.23	0.33	0.54
2349	34	21	rainy	0.23	0.36	0.56
2361	36	24	cloudy	0.33	0.42	0.60
2379	30	24	rainy	−0.09	−0.17	0.47
2391	35	23	cloudy	0.20	0.32	0.58
2408	33	23	rainy	0.15	0.24	0.54
2439	28	19	sunny	0.04	0.05	0.49
2453	23	17	rainy	0.00	−0.03	0.46
2472	18	14	rainy	0.07	0.14	0.53
2483	22	18	rainy	−0.03	−0.07	0.49
2501	16	9	rainy	−0.10	−0.17	0.54
2514	21	12	cloudy	−0.08	−0.13	0.51
2531	16	4	cloudy	−0.11	−0.21	0.59
2532	14	5	cloudy	−0.11	−0.21	0.59
2544	11	8	rainy	−0.19	−0.24	0.58
2561	13	8	sunny	−0.17	−0.22	0.57
2572	10	4	sunny	−0.21	−0.25	0.62
2592	13	8	rainy	−0.16	−0.21	0.57
2620	13	6	sunny	−0.03	−0.07	0.50
2638	15	8	sunny	−0.20	−0.26	0.58
2663	28	14	cloudy	0.15	0.20	0.50
2669	23	14	rainy	0.12	0.18	0.50
2680	23	13	rainy	0.21	0.32	0.58
2689	33	17	cloudy	0.29	0.46	0.67
2712	31	18	cloudy	0.32	0.49	0.72
2725	28	20	cloudy	0.30	0.48	0.70
2741	28	21	rainy	0.13	0.23	0.55
2755	31	24	rainy	0.37	0.54	0.76
2773	33	24	sunny	0.48	0.66	0.88

References

[1] People's Republic of China Ministry of Railways. Code for design of high speed railways, TB 10621-2009/J 971-2009. China Railway Press; 2009 [in Chinese].
[2] S.L. Sun, Design and practice of high speed railway bridge, China Railway Press (2011).
[3] B. Yan, G.L. Dai, N. Hu, Recent development of design and construction of short span high-speed railway bridges in China, Eng. Struct. 100 (2015) 707–717.
[4] D. Cantero, M. Ülker-Kaustell, R. Karoumi, Time–frequency analysis of railway bridge response in forced vibration, Mech. Syst. Sig. Process. 76–77 (2016) 518–530.
[5] M. Gao, J. Cong, P. Wang, et al, Dynamic modeling and experimental investigation of self-powered sensor nodes for freight rail transport, Appl. Energy 257 (2020) 113969.
[6] M. Gao, Y. Wang, Y. Wang, P. Wang, Y. Sun, J. Xiao, Modeling and experimental verification of a fractionally damped quad-stable energy harvesting system for use in wireless sensor networks, Energy 190 (2020) 116301.
[7] M. Gao, C. Su, J. Cong, F. Yang, Y. Wang, P. Wang, Harvesting thermoelectric energy from railway track, Energy 180 (2019) 315–329.
[8] M. Gao, Y. Wang, Y. Wang, et al, Experimental investigation of non-linear multi-stable electromagnetic- induction energy harvesting mechanism by magnetic levitation oscillation, Appl. Energy 220 (2018) 856–875.
[9] C. Carey, E.J. Obrien, A. Malekjafarian, et al, Direct field measurement of the dynamic amplification in a bridge, Mech. Syst. Sig. Process. 85 (2017) 601–609.
[10] P. Lou, Z.W. Yu, F.T.K. Au, Rail–bridge coupling element of unequal lengths for analysing train–track–bridge interaction systems, Appl. Math. Model. 36 (4) (2012) 1395–1414.
[11] S. Zhou, G. Song, R. Wang, et al, Nonlinear dynamic analysis for coupled vehicle-bridge vibration system on nonlinear foundation, Mech. Syst. Sig. Process. 87 (2017).
[12] A. Gupta, A.S. Ahuja, Dynamic Analysis of Railway Bridges under High Speed Trains, Universal J. Mech. Eng. 2 (6) (2014) 199–204.
[13] M. Jahangiri, J.A. Zakeri, Dynamic analysis of train-bridge system under one-way and two-way high-speed train passing, Struct. Eng. Mech. 64 (1) (2017) 33–44.
[14] P. Museros, M.L. Romero, A. Poy, et al, Advances in the analysis of short span railway bridges for high-speed lines, Comput. Struct. 80 (27–30) (2002) 2121–2132.
[15] M. Tanabe, M. Sogabe, H. Wakui, N. Matsumoto, Y. Tanabe, Exact Time Integration for Dynamic Interaction of High-Speed Train and Railway Structure Including Derailment During an Earthquake, J. Comput. Nonlinear Dynam 11 (3) (2016) 031004.
[16] P.A. Montenegro, S.G.M. Neves, R. Calçada, M. Tanabe, M. Sogabe, Wheel rail contact formulation for analyzing the lateral train-structure dynamic interaction, Comput. Struct. 152 (2015) 200–214.
[17] P.A. Montenegro, R. Calçada, N. Vila Pouca, M. Tanabe, Running safety assessment of trains moving over bridges subjected to moderate earthquakes, Earthquake Eng. Struct. Dyn. 45 (2016) 483–504.
[18] P.A. Montenegro, H. Carvalho, R. Calçada, A. Bolkovoy, I. Chebykin, Stability of a train running over the Volga River high speed railway bridge during crosswinds, Struct. Infrastruct. Eng. (2019).
[19] T. Arvidsson, R. Karoumi, Train-bridge interaction - a review and discussion of key model parameters, Int. J. Rail Trans. 2 (3) (2014) 147–186.
[20] H. Xia, W.W. Guo, N. Zhang, G.J. Sun, Dynamic analysis of a train-bridge system under wind action, Comput. Struct. 86 (2008) 1845–1855.
[21] J.M. Rocha, A.A. Henriques, C. Rui, Probabilistic assessment of the train running safety on a short-span high-speed railway bridge, Struct. Infrastruct. Eng. 12 (1) (2016) 78–92.
[22] J.M. Rocha, A.A. Henriques, R. Calçada, Safety assessment of a short span railway bridge for high-speed traffic using simulation techniques, Eng. Struct. 40 (7) (2012) 141–154.
[23] W.Q. Li, Y. Zhu, X.Z. Li, Dynamic Response of Bridges to Moving Trains: A Study on Effects of Concrete Creep and Temperature Deformation, Appl. Mech. Mater. 193–194 (2012) 1179–1182.
[24] H. Ouyang, Moving-load dynamic problems: A tutorial (with a brief overview), Mech. Syst. Sig. Process. 25 (6) (2011) 2039–2060.
[25] M.A. Rosa, J.F. Stanton, M.O. Eberhard, Improving Predictions for Camber in Precast, Prestressed Concrete Bridge Girders. University of Washington, Washington State Transportation Center (TRAC), 2007.
[26] S. Rizkalla, P. Zia, T. Storm. Predicting Camber, Camber, and Prestress Losses in Prestressed Concrete Members. North Carolina State University, 2011.
[27] C. O'Neill, C. French, Validation of Prestressed Concrete I-Beam Camber and Camber Estimates, University of Minnesota, Department of Civil Engineering, 2012.
[28] M.A. Rosa, J.F. Stanton, Improving Predictions for Camber in Precast, Prestressed Concrete Bridge Girders, Concrete (2007).
[29] S. Rizkalla, P. Zia, T. Storm. Predicting Camber, Deflection, and Prestress Losses in Prestressed Concrete Members. Bridge Design, 2011.
[30] J.M. Stallings, Camber and Prestress Losses in Alabama HPC Bridge Girders, PCI J. 48 (2003).
[31] H. Guo-jing, L. Yuan-yuan, Zhong-quan Zou, et al, Effect of concrete creep on pre-camber of continuous rigid-frame bridge, J. Central South University 15 (s1) (2008) 337–341.
[32] T.K. Storm, S.H. Rizkalla, P.Z. Zia, Effects of production practices on camber of prestressed concrete bridge girders, PCI J. 58 (1) (2013) 96–111.
[33] Z. Chen, L. Li, X. Xiao, GM(1,1) Model and Its Application to Controlling the Inverted Camber of Widening Concrete Bridge, J. Grey System (2006).
[34] Z. Li, K. Deng, Y. Li, et al, Research on Concrete Creep and Application in Pre-camber Setup of Bridge, Trans. Sci. Tech. (2006).
[35] S.P. Gross, Camber of High Strength Concrete Bridge Girders, Hpc Bridge Views (2005).
[36] H. Wenjun, Creep and Shrinkage of High Performance Concrete, and Prediction of Long-Term Camber of Prestressed Bridge Girders, Graduate Theses and Dissertations, Iowa State University, 2013.
[37] J. Karthikeyan, Long-term effects due to creep and shrinkage on prestressed concrete bridge girders using SCC, Int. J. Struct. Eng. 2 (4) (2011) 390–403.
[38] T.E. Cousins, Investigation of Long-Term Prestress Losses in Pretensioned High Performance Concrete Girders, Virginia Transportation Research Council. (2005).
[39] C. Czaderski, M. Motavalli, 40-Year-old full-scale concrete bridge girder strengthened with prestressed CFRP plates anchored using gradient method, Compos. B 38 (7) (2007) 878–886.
[40] M.K. Tadros, Precast, prestressed girder camber variability, PCI J. (2011) 135–154.
[41] G.X. Ning, D.Y. Kong, P.Z. Lin, et al, Camber Analysis of a Whole PC Box Girder on Double-track Railway, J. China Railway Society (2007).
[42] D. Feng, S.M. Asce, M.Q. Feng, et al, Model Updating of Railway Bridge Using in Situ Dynamic Displacement Measurement under Trainloads, J. Bridge Eng. 20 (12) (2015).
[43] G.Q. Li, X.B. Liu, F. Yang, et al, Variation law and impact on dynamic performance of profile irregularity caused by creep of simply-supported beams on High-speed railways (in Chinese), Scientia Sinica Technologica 44 (2014) 786–792.
[44] P.J. Barr, J.F. Stanton, M.O. Eberhard, Effects of Temperature Variations on Precast, Prestressed Concrete Bridge Girders, J. Bridge Eng. 10 (2) (2005) 186–194.
[45] M.K. Tadros, N. Al-Omaishi, Prestressed losses in pretensioned high-strength concrete bridge girders, Transportation Research Board, Washington D. C., 2003.
[46] N. Ranaivomanana, S. Multon, A. Turatsinze, Basic creep of concrete under compression, tension and bending, Constr. Build. Mater. 38 (1) (2013) 173–180.
[47] Jonathan E. Sanek, Field Verification of Camber Estimates for Prestressed Concrete Bridge Girders, University of Florida, 2005.

[48] L. Carin, Roberts-Wollman, J.E. Breen, at al. Measurements of Thermal Gradients and their Effects on Segmental Concrete Bridges. J. Bridge Eng., 7 (3) (2002) 166–174.
[49] N. Currier, Validation of Stresses Caused by Thermal Gradients in Segmental Concrete Bridges - Phase II, Ann. Hematol. 64 (1 Supplement) (2009) A137–A139.
[50] I. Gonzalez, R. Karoumi, Analysis of the annual variations in the dynamic behavior of a ballasted railway bridge using Hilbert transform, Eng. Struct. 60 (C) (2014) 126–132.
[51] I. Gonzales, M. Ülker-Kaustell, R. Karoumi, Seasonal effects on the stiffness properties of a ballasted railway bridge, Eng. Struct. 57 (C) (2013) 63–72.
[52] P. Moser, B. Moaveni, Environmental effects on the identified natural frequencies of the Dowling Hall Footbridge, Mech. Syst. Signal Process. 25 (7) (2011) 2336–2345.
[53] J. Guo, C. Zhu, Dynamic displacement measurement of large-scale structures based on the Lucas-Kanade template tracking algorithm, Mech. Syst. Sig. Process. s 66–67 (2016) 425–436.
[54] AASHTO. Interim Revisions to the Guide Specifications for Design and Construction of Segmental Concrete Bridges, Second Edition, Washington, D.C. 2003.
[55] AASHTO. Guide specifications for design and construction of segmental concrete bridges, 2nd Ed., Washington, D.C. 1999.
[56] M. Moravcik, L. Krkoska, Thermal Effects on Box Girder Concrete Bridges, Key Eng. Mater. 738 (2017) 273–283.
[57] I.C. Potgieter, W.L. Gamble, Response of highway bridges to nonlinear temperature distributions. Rep. No. FHWA/IL/ UI-201, Univ. of Illinois at Urbana-Champaign, Urbana-Champaign, Ill. 1983.
[58] A. Haigermoser, B. Luber, J. Rauh, G. Gräfe, Road and track irregularities: measurement, assessment and simulation, Veh. Syst. Dyn. 53 (7) (2015) 878–957.
[59] Jens Nielsen, Eric Berggren, Overview of Methods for Measurement of Track Irregularities Important for Ground-Borne Vibration, RIVAS CHALMERS WP2 Deliverable D2 (2013) 5.
[60] M. Bocciolone, A. Caprioli, A. Cigada, A. Collina, A measurement system for quick rail inspection and effective track maintenance strategy, Mech. Syst. Sig. Process. 21 (3) (2007) 1242–1254.
[61] P. Wang, Y. Wang, H. Tang, et al, Error Theory of Chord-based Measurement System regarding Track Geometry and Improvement by High Frequency Sampling, Measurement 115 (2017) 204–216.
[62] Y. Wang, H. Tang, P. Wang, et al, Multipoint Chord Reference System for Track Irregularity: Part I –Theory and Methodology, Measurement 138 (2019) 240–255.
[63] Y. Wang, H. Tang, P. Wang, et al, Multipoint Chord Reference System for Track Irregularity: Part II – Numerical Analysis, Measurement 138 (2019) 194–205.
[64] Z.F. Cao, W.J. Chen, L. Chong, et al, The Review of Track Inspection Technology and Application Prospect on Subway, Appl. Mech. Mater. 635–637 (2014) 805–810.
[65] M. Mishra, J. Odelius, A. Thaduri, et al, Particle filter-based prognostic approach for railway track geometry, Mech. Syst. Sig. Process. (2017) 226–238.
[66] G. Perrin, D. Duhamel, C. Soize, et al, Quantification of the influence of the track geometry variability on the train dynamics, Mech. Syst. Sig. Process. 60–61 (2015) 945–957.
[67] Y. Wang, P. Wang, X. Wang, et al, Position synchronization for track geometry inspection data via big-data fusion and incremental learning, Transp. Res. Part C: Emerg. Tech. 93 (8) (2018) 544–565.
[68] G. Perrin, C. Soize, D. Duhamel, et al, Track irregularities stochastic modeling, Probab. Eng. Mech. 34 (34) (2013) 123–130.
[69] A. Bossio, T. Monetta, F. Bellucci, et al, Modeling of concrete cracking due to corrosion process of reinforcement bars, Cem. Concr. Res. 71 (2015) 78–92.
[70] J. Zhong, P. Gardoni, D. Rosowsky, Stiffness Degradation and Time to Cracking of Cover Concrete in Reinforced Concrete Structures Subject to Corrosion, J. Eng. Mech. 136 (2) (2010) 209–219.
[71] M. Gao, P. Wang, L. Jiang, B. Wang, et al, Power generation for wearable systems, Energy & Environmental Science (2021), https://doi.org/10.1039/D0EE03911J.
[72] Y. Sun, P. Wang, J. Lu, et al, Rail corrugation inspection by a self-contained triple-repellent electromagnetic energy harvesting system, Applied Energy 286 (3) (2021) 116512, https://doi.org/10.1016/j.apenergy.2021.116512.